

Clustering of floating tracer due to mesoscale vortex and submesoscale fields

Dmitry V. Stepanov¹, Eugene A. Ryzhov¹, Alexei A. Zagumennov³, Pavel Berloff², Konstantin V. Koshel¹

¹V.I.Ilichev Pacific Oceanological Institute of FEB RAS, 43, Baltiyskaya Street, Vladivostok, 690041,

Russia

²Department of Mathematics, Imperial College London, London, SW7 2AZ, United Kingdom

³Institute of Automation and Control Processes FEB RAS, 5, Radio Street, Vladivostok, 690041, Russia

Key Points:

- Phenomenology of floating tracer clustering in the divergent submesoscale and mesoscale flow;
- Exponential clustering process is analyzed depending on the submesoscale model characteristics.
- It is argued that the 2D velocity field divergence is essential for studying tracer transport properties.

Corresponding author: Dmitry Stepanov, step-nov@poi.dvo.ru

-1-

This article has been accepted for publication and undergone full peer review but has not been through the copyediting, typesetting, pagination and proofreading process, which may lead to differences between this version and the Version of Record. Please cite this article as doi: 10.1029/2019GL083111

Abstract

Floating tracer clustering is studied in oceanic flows that combine both a field of coherent mesoscale vortices, as simulated by a regional, comprehensive, eddy-resolving general circulation model, and kinematic random submesoscale velocity fields. Both fields have rotational and divergent velocity components, and depending on their relative contributions, as well as on the local characteristics of the mesoscale vortices, we identified different clustering scenarios. We found that the mesoscale vortices do not prevent clustering but significantly modify its rate and spatial pattern. We also demonstrated that even weak surface velocity divergence has to be taken into account to avoid significant errors in model predictions of the floating tracer patterns. Our approach combining dynamically constrained and random velocity fields, and the applied diagnostic methods, are proposed as standard tools for analyses and predictions of floating tracer distributions, both in observational data and general circulation models. **Plain language summary**

The problem of dispersion and aggregation of various tracers in the ocean has recently attracted a lot of interest. These tracers can be natural ocean water characteristics, such as temperature and salinity, or various hazardous impurities, such as plastic pollution and oil spills. The latter tracers are also the floating ones, which means that their dynamics is different from the passive tracers. An important and interesting aspect of the floating tracers is their ability to form pronounced clusters, that is aggregations in isolated patches — understanding and predicting this phenomenon is one of the challenges in modern oceanography. In this study we explore how floating-tracer clustering depends on kinematic characteristics of the ocean surface velocity.

1 Introduction

Mesoscale eddies are a ubiquitous component of the ocean circulation that significantly contributes to the material transport of oceanic properties and tracers, such as density, salinity, marine life and pollution. The corresponding background literature is immense, and the theoretical aspects are comprehensively reviewed in (McWilliams, 2008; Samelson, 2013). For the purposes of this study, we note that coherent mesoscale vortices constitute substantial part of the total eddy field (Barbosa Aguiar, Peliz, & Carton, 2013; Chelton, Schlax, & Samelson, 2011; Chelton, Schlax, Samelson, & de Szoeke, 2007; Martínez-Moreno, Hogg, Kiss, Constantinou, & Morrison, 2019), contribute significantly to the material transport, and are remarkably long-lived and structurally organized, as opposed to more random and wave-like eddies around them.

Ocean circulation at the scales smaller than the mesoscale is dominated by the broad range of submesoscale processes, which have been intensively studied (Berta, Griffa, Özgökmen, & Poje, 2016; Berti, Santos, Lacorata, & Vulpiani, 2011; Haza, Özgökmen, & Hogan, 2016; Huntley, Lipphardt Jr., Jacobs, & Kirwan Jr., 2015; Jacobs et al., 2016; McWilliams, 2016; Ohlmann, Romero, Palls-Sanz, & Perez-Brunius, 2019; Schroeder et al., 2012; Zhong & Bracco, 2013). Interactions between submesoscale and mesoscale motions are essential in the formation and breakdown of coherent mesoscale vortices, but the theoretical understanding is hindered by overwhelming computational costs due to the spatial resolution requirements (Dauhajre, McWilliams, & Renault, 2019). An efficient way (though, with obvious limitations) to study these interactions is by employing kinematic models for submesoscales, whereas retaining dynamical models for mesoscales — this is the approach adopted in our study and applied to the tracer clustering phenomena.

Although, it is well-established that floating tracers tend to form spatially localised aggregations (Cozar et al., 2014; Law et al., 2010; Martinez, Maamaatuaiahutapu, & Tailandier, 2009; Maximenko, Hafner, & Niiler, 2012; McComb, 1990; Okubo, 1980; Väli, Zhurbas, Laanemets, & Lips, 2018) referred to as *clusters*, their definitions and measures of the degree of clustering differ substantially (Huntley et al., 2015; Jacobs et al., 2016).

67 Dynamics of *floating* tracers is fundamentally different from the dynamics of *passive* trac-
 68 ers, because in the former case the tracer density on fluid particles changes due to the
 69 experienced surface-velocity divergence, whereas in the latter case it is materially con-
 70 served and only advected by the flow. In other words, the floating-tracer density is com-
 71 pressible and can not be fully described by concentrations of Lagrangian particles — this
 72 fundamental theoretical issue escaped attention of many previous studies that dealt with
 73 the Lagrangian transport on the ocean surface (Cedarholm, Rypina, Macdonald, & Yoshida,
 74 2019; Olascoaga et al., 2013; Prants, Budyansky, & Uleysky, 2018; Wang, Olascoaga, &
 75 Beron-Vera, 2015). Physical mechanisms leading to formation of clusters can be differ-
 76 ent and overall remain poorly understood. This study deals with clustering due to the
 77 surface-velocity divergence, which is present in both mesoscale and submesoscale mo-
 78 tions.

79 We focus on tracers *floating* on the ocean surface and, therefore, directly experi-
 80 encing only the 2D surface velocity. We define clusters as small and transient areas that
 81 exponentially shrink in time and collect the exponentially growing in time fraction of the
 82 tracer (Isichenko, 1992; Klyatskin & Koshel, 2000). The asymptotic theory of cluster-
 83 ing in random velocity fields (Klyatskin, 2015) states that the exponential clustering oc-
 84 curs necessarily, if the divergent velocity component completely dominates over the ro-
 85 tational one. When both components are comparable, the exponential clustering per-
 86 sists but its properties become significantly altered (Koshel, Stepanov, Ryzhov, Berloff,
 87 & Klyatskin, 2019) — this result is, however, restricted to specific and purely kinematic
 88 velocities. The main novelty of the present work is in relaxing this restriction by dynam-
 89 ically constraining the mesoscale flow component, which is referred to as the regular com-
 90 ponent. The random velocity field modelling the submesoscales represents ~ 200 – 2000
 91 m scales, has the surface divergence, which is 2 orders of magnitude larger than that of
 92 the mesoscales, is controlled by only 2 parameters: correlation radius and variance.

93 This Letter aims at establishing phenomenology of possible floating-tracer cluster-
 94 ing scenarios depending on the submesoscale divergent flow component in the presence
 95 of dynamically modeled coherent mesoscale vortices.

96 2 Models

97 In this section we discuss the submesoscale and mesoscale velocity models, and how
 98 the tracer density fields were obtained.

99 Floating tracer is advected by a 2D flow with velocity $\mathbf{U}(\mathbf{R}, t) = (u(\mathbf{r}, t), v(\mathbf{r}, t))|_{z=0}$
 100 characterized by the divergence

$$\nabla_{\mathbf{R}}\mathbf{U}(\mathbf{R}, t) = -\frac{\partial w(\mathbf{r}, t)}{\partial z}|_{z=0}, \quad (1)$$

101 where $\mathbf{r} = (x, y, z)$ is the full position vector; $\mathbf{R} = (x, y)$ is the horizontal position vec-
 102 tor; $\nabla_{\mathbf{R}}\mathbf{U}(\mathbf{R}, t)$ is the horizontal divergence at the ocean surface ($z = 0$); and $w(\mathbf{r}, t)$
 103 is the vertical velocity component.

104 Since there is no vertical flux of the floating tracer, the evolution of its density $\rho(\mathbf{r}, t)$
 105 is governed by the conservation law:

$$\left(\frac{\partial}{\partial t} + \nabla_{\mathbf{R}}\mathbf{U}(\mathbf{R}, t)\right)\rho(\mathbf{R}, t) = 0, \quad \rho(\mathbf{R}, 0) = \rho_0(\mathbf{R}), \quad (2)$$

106 and the total mass of the tracer is conserved: $M = \int d\mathbf{R}\rho(\mathbf{R}, t) = \text{const}$. We treat
 107 (2) and the velocity field in a nondimensional form, with the space, time and density scales
 108 denoted as L_0 , t_0 and ρ^* , respectively, and chosen to be the typical mesoscale eddy size
 109 (i.e., of the order of the first baroclinic Rossby radius) and turnover time, and the ini-
 110 tial density (distributed over the unity size area); and the velocity scale follows from this
 111 as $U^* = L_0/t_0$.

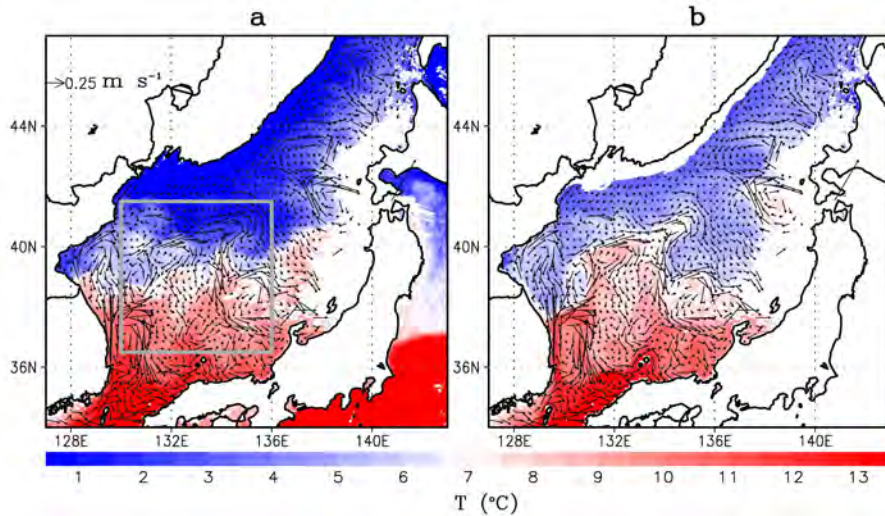


Figure 1: Monthly mean (March 2000) sea surface mesoscale velocity field (regular component) from the Japan/East Sea circulation model; the corresponding monthly mean sea surface temperature (colour shading, in degrees of Celsius) from (a) satellite observations and (b) model. The general circulation patterns are reliably captured by the simulation, so that the warm and cold regions of the JES are separated by the intense meandering jet and its adjacent vortices. The grey square indicates the subdomain of interest.

2.1 Mesoscale velocity model

The mesoscale (regular) component is a solution of an eddy-resolving (1/12-degree), regional, hydrostatic Boussinesq, sigma-coordinate, INMOM model (Diansky, Stepanov, Gusev, & Novotryasov, 2016; Stepanov, Diansky, & Novotryasov, 2014) configured for the Japan/East Sea (JES) region plus the Sea of Okhotsk and adjacent parts of the Pacific Ocean. It is driven by the atmospheric forcing provided by the JRA55-do dataset covering the 1958–2017 period, and incorporating climatological boundary conditions on the open boundaries of the domain (Stepanov, Diansky, & Fomin, 2018). The simulated solution is averaged over one-month intervals (Fig. 1b), and one of its surface velocity snapshots (March 2000) in the south-western JES region is used for the follow-up analyses. To validate the simulated velocity field, we overlaid it with the corresponding monthly mean sea surface temperature (SST) data provided by the AVHRR (Advanced Very-High-Resolution Radiometer) mounted on the satellites NOAA-12 and NOAA-15. The simulated circulation of the JES is consistent with the existing observations (Diansky et al., 2016; Stepanov et al., 2014).

We picked up the subdomain containing pronounced vortices with horizontal shears (grey square in Fig. 1 corresponds to the vorticity field (left panel) and the divergence field (right panel) in Fig. 2). The locations of interest, designated (Fig. 2) by C_1 (cyclonic eddy), A_2 (two weak anticyclonic eddies) and A_1 (cyclone and anticyclone pair), serve as typical eddy configurations with their distinct material transport patterns. At this stage we are interested in clustering phenomena developing much faster than the characteristic time scale of the mesoscale (regular) velocity field — this justifies our use of the stationary mesoscale flow.

In dimensional units, the random velocity scale is 2.0 m/s , whilst the characteristic regular velocity is of the order of magnitude smaller, i.e., about 0.2 m/s . The characteristic divergence of the regular velocity is about 10^{-6} s^{-1} (see the top-right panel

icle

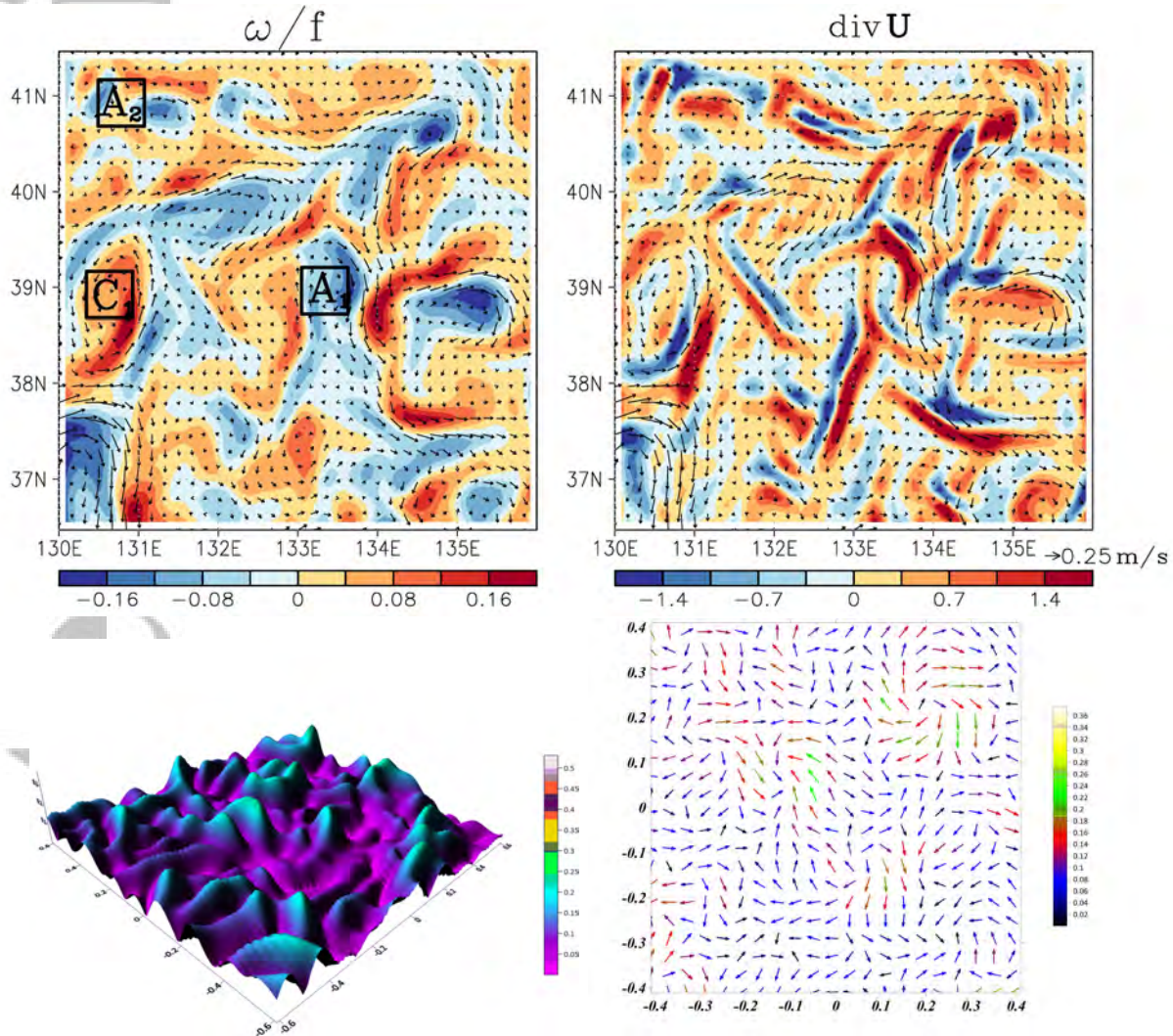


Figure 2: Top row: regular (mesoscale) flow fields. Left panel: vertical component of the relative vorticity vector normalized by the local Coriolis parameter; right panel: surface-velocity divergence (units are $10^{-6} s^{-1}$). The squares labelled as A_1 , A_2 and C_1 denote the tracer deployment regions. Bottom row: snapshots of the random flow properties in a zoomed in subdomain, and for $\gamma = 0.5$. Left panel: the corresponding flow speed; right panel: the corresponding random velocity field (color-coded).

AC

138 in Fig. 2), whilst the random velocity divergence is orders of magnitude larger, i.e., about
 139 10^{-2} s^{-1} .

140 2.2 Submesoscale velocity model

141 The 2D divergent velocity field \mathbf{U} is random, normally distributed, spatially ho-
 142 mogeneous, isotropic, and stationary; it is also a linear combination of the modelled mesoscale
 143 mean, and the submesoscale divergent and rotational components:

$$\mathbf{U}(\mathbf{R}, t) = \underbrace{\langle \mathbf{U}(\mathbf{R}, t) \rangle}_{\text{mesoscale}} + \underbrace{\gamma \mathbf{U}^p(\mathbf{R}, t) + (1 - \gamma) \mathbf{U}^s(\mathbf{R}, t)}_{\text{submesoscale}}, \quad (3)$$

144 where superscript p indicates the divergent (irrotational) component, superscript s in-
 145 dicates the rotational (nondivergent) component, and parameter $0 \leq \gamma \leq 1$ sets their
 146 relative contributions.

147 Our next goal is to formulate a model for random, spatially correlated, and tem-
 148 porally uncorrelated (i.e., δ -correlated), kinematic velocity field; for this purpose we de-
 149 fine (Klyatskin, 1994, 2015) the correlation tensor:

$$B_{\alpha\beta}^j(\mathbf{R}', \eta) = \langle U_{\alpha}^j(\mathbf{R}, t) U_{\beta}^j(\mathbf{R} + \mathbf{R}', t + \eta) \rangle = \int d\mathbf{k} E_{\alpha\beta}^j(\mathbf{k}, \eta) e^{i\mathbf{k}\mathbf{R}'}, \quad (4)$$

150 where indices α and β stand for x and y and indicate different components of the ten-
 151 sor; and index j stands for p and s , and indicates different tensors; and the following spec-
 152 tral densities are assumed:

$$E_{\alpha\beta}^p(\mathbf{k}, \eta) = E^p(k, \eta) \frac{k_{\alpha} k_{\beta}}{k^2}, \quad E_{\alpha\beta}^s(\mathbf{k}, \eta) = E^s(k, \eta) \left(\delta_{\alpha\beta} - \frac{k_{\alpha} k_{\beta}}{k^2} \right). \quad (5)$$

153 The correlation tensor is nonzero only for the zero time lag η :

$$B_{\alpha\beta}^j(\mathbf{0}, 0) = \langle U_{\alpha}^j(\mathbf{R}, t) U_{\beta}^j(\mathbf{R}, t) \rangle = \frac{1}{2} \left(\sigma_{\mathbf{U}}^j \right)^2 \delta_{\alpha\beta}, \quad (6)$$

154 where $\left(\sigma_{\mathbf{U}}^j \right)^2 = B_{\alpha\alpha}^j(\mathbf{0}, 0) = \int d\mathbf{k} E^j(k, 0)$. In our case we take $E^s = E^p = E$, and
 155 the spectral density is taken as

$$E(k, 0; l) = \frac{1}{2\pi} \frac{l^4}{4} k^2 \exp \left\{ -\frac{1}{2} k^2 l^2 \right\}, \quad (7)$$

156 where l is the spatial correlation radius parameter. In numerical simulations, we use ran-
 157 dom phase, $\sigma_{\mathbf{U}}^p = \sigma_{\mathbf{U}}^s \simeq 0.1$, which results in the typical velocity of 0.2 m/s , $l = 0.08$
 158 (i.e., 2.0 km), and time step 0.01 (i.e., 120 s).

159 2.3 Numerical implementation and methodology

160 We simulated the random velocity spectrally on uniform 2048×2048 grid (Kly-
 161 atskin & Koshel, 2017), and the regular velocity component is taken to be piecewise-constant
 162 over the same grid. Since the random field is not differentiable in time, we solve the La-
 163 grangian equivalent of (2),

$$\begin{aligned} \frac{d\mathbf{R}}{dt} &= \mathbf{U}(\mathbf{R}, t), \quad \mathbf{R}(0) = \xi, \\ \frac{d\rho}{dt} &= -\nabla_{\mathbf{R}} \mathbf{U}(\mathbf{R}, t) \rho(t), \quad \rho(0) = \rho_0(\xi), \end{aligned} \quad (8)$$

164 as applied to ensembles of Lagrangian particles advected by the total velocity field and
 165 solved numerically by the method of characteristics (Klyatskin, 1994, 2015; Koshel & Alexan-
 166 drova, 1999), where ξ is the initial position of each particle. Equations (8) are time-stepped

167 using the standard Euler-Itô scheme (Kloeden & Platen, 1992; Klyatskin & Koshel, 2017;
 168 Koshel & Alexandrova, 1999), and the Eulerian density field can be obtained by the spa-
 169 tial coarse-graining, if needed.

170 To analyze the clustering we employed the statistical topography methodology (Isichenko,
 171 1992). One of the characteristics used in statistical topography is the *clustering area*, which
 172 is defined as the total combined area of the regions where the tracer density exceeds cer-
 173 tain threshold:

$$\langle S(t; \bar{\rho}) \rangle = \int d\mathbf{R} \langle \theta(\rho(\mathbf{R}, t) - \bar{\rho}) \rangle = \int d\mathbf{R} \int_{\bar{\rho}}^{\infty} d\rho' P(\mathbf{R}, t; \rho'), \quad (9)$$

174 where $\theta(\cdot)$ is the Heaviside (step) function; and $P(\mathbf{R}, t; \rho)$ is the probability density func-
 175 tion (PDF) of the tracer density. The other useful characteristics is the *clustering mass*,
 176 which is the amount of tracer aggregated within the clustering area:

$$\langle M(t; \bar{\rho}) \rangle = \int d\mathbf{R} \rho(\mathbf{R}, t) \langle \theta(\rho(\mathbf{R}, t) - \bar{\rho}) \rangle = \int d\mathbf{R} \int_{\bar{\rho}}^{\infty} d\rho' \rho' P(\mathbf{R}, t; \rho'). \quad (10)$$

177 In the exponential clustering regime, the clustering area tends to zero, and the cluster-
 178 ing mass tends to unity (i.e., clusters accumulate all the available tracer) in the large-
 179 time limit (Klyatskin, 2015; Klyatskin & Koshel, 2017). The exact analytical estimates
 180 for the clustering area and mass are derived in (Klyatskin, 2015) for purely divergent ve-
 181 locity case:

$$\langle S(t; \bar{\rho}) \rangle \sim \exp(-\frac{1}{4}\tau)/\sqrt{\tau} = \exp(-\frac{1}{4}D_p t)/\sqrt{D_p t}, \quad \langle M(t; \bar{\rho}) \rangle \sim 1 - \langle S(t; \bar{\rho}) \rangle, \quad (11)$$

182 where $D_p = (\gamma^2 \sigma_U^2 / l^2) t_0$ is the effective diffusivity of the divergent velocity component.
 183 Most of our numerical simulations were carried out with $\sigma_U = 0.1$ and $l = 0.08$; and
 184 for this set of parameters, we use notation D_0 instead of D_p .

185 We distribute 3 square-shaped tracer patches in the subdomain of interest (Fig. 2),
 186 and each tracer patch contains 36×10^6 uniformly distributed Lagrangian particles. This
 187 number of particles has been tested (by doubling and halving) and found adequate in
 188 capturing the clustering characteristics of interest; moreover, when we considered a purely
 189 divergent and no-mean velocity field ($\gamma = 1$), the numerical solution matched the cor-
 190 responding asymptotic estimate (11). Four experiments have been devised with the same
 191 regular velocity and different random velocity fields:

- 192 1. EXP1 employs only the regular velocity field and forms the reference solution to
- 193 evaluate the effect of the submesoscale further;
- 194 2. EXP2 — plus the purely rotational random velocity field ($\gamma = 0$);
- 195 3. EXP3 — plus the purely divergent random velocity field ($\gamma = 1$);
- 196 4. EXP4 — plus the mixed random velocity field ($\gamma = 0.5$).

197 3 Clustering scenarios

198 The reference case EXP1 (i.e., with the random submesoscale component switched
 199 off) illustrates typical tracer patterns in the deployment regions (Fig. 3a). Stationary
 200 vortices retain the tracer; in the regions with no closed streamlines, the tracer is intensely
 201 stirred and spread out; large values of tracer density are rare and correspond to the sinks
 202 in the flow field.

203 Now, we turn our attention to the benchmark solutions (EXP2, EXP3, and EXP4)
 204 featuring different submesoscale flow components. The purely rotational EXP2 solution

(Fig. 3b) is characterized by smearing of the tracer patches due to enhanced tracer dispersion. Similar effect has been observed in the model of an isolated ellipsoidal vortex subject to random velocity perturbations (Koshel, Ryzhov, & Zhmur, 2013). Overall tracer patterns and density values are similar to EXP1 (Fig. 3a), but the boundaries of the tracer patches are more filamented due to the random fluctuations.

When the random velocity field is purely divergent (EXP3; $\gamma = 1$; Fig. 3c), the tracer evolution is characterized by the exponential clustering (followed up to the two orders of magnitude density increase). On the other hand, the overall large-scale pattern of the mesoscale-size tracer features, that is clearly seen in the other experiments, is significantly eroded. Remarkably, the exponential clustering develops even within the intensively sheared mesoscale jet and vortices (entirely from vortex peripheries to cores). Somewhat similar but grainy small-scale pattern is found when amplitudes of the rotational and divergent submesoscale flow components are equal (EXP4; $\gamma = 0.5$): the tracer evolution is also characterized by the exponential clustering (Fig. 3d), and the large-scale tracer distribution pattern is like in EXP1 and EXP2.

Since our interest is mostly in the clustering process subject to coherent mesoscale vortices, we choose a typical situation — the cyclone over C_1 deployment location — and analyze the corresponding tracer evolution in detail (Fig. 4). In EXP1 the tracer is expelled towards periphery of the cyclone; in EXP2 it is additionally smeared across the mesoscale shear, and the boundary of the tracer patch is significantly more distorted; in EXP3 the exponential clustering is most pronounced (Figs. 3–4); in EXP4 despite the strong influence of the rotational component, the exponential clustering still persists; qualitative difference between the clustering dynamics in EXP3 and EXP4 are discussed in the next section. Note, that clusters tend to aggregate differently in cyclones (tendency towards the periphery) and anticyclones (tendency towards the centre); e.g., consider A_1 , where clusters fill up the anticyclone's centre.

For a partial interpretation of the modeling results, we resort to the asymptotic theory of clustering in random velocity fields containing uniform-shear flow component (Klyatskin, 2015), which predicts the following time dependence of the single-particle dispersion:

$$\sigma_{xx}^2 = 2D_0t(1 + \alpha t + \frac{1}{3}\alpha^2 t^2), \quad \sigma_{yy}^2 = 2D_0t, \quad (12)$$

where α is the shear parameter. According to this estimate, a tracer patch should be smeared in time, and more so along the shear direction (Fig. 3b); but in the case of purely rotational velocity (i.e., there is no exponential clustering), there is an estimate for the dispersion of the density gradient p (Klyatskin, 2015):

$$\langle p^2(t) \rangle \sim \exp \left\{ \left(\frac{3}{2} \alpha^2 D_s \right)^{1/3} t \right\}, \quad (13)$$

where D_s is the variation due to the purely rotational random velocity field. This estimate is obtained in the limit $D_s \ll \alpha$, when $\alpha \neq 0$, and its interpretation is as follows: regardless of how small D_s is, it still contributes towards increasing the gradient dispersion, that is, it makes the tracer patch boundary more serrated (similar tendencies are seen in Fig. 3b), opposite to the (elongating) effect of uniform shear on the tracer patch. Although, the above estimate is valid for uniform shear, we expect it to be true for more complicated shears, and this expectation is consistent with the solutions discussed in this section.

To quantify clustering properties in the above-discussed scenarios, we make use of statistical topography diagnostics, such as the clustering area and mass. In EXP4 the rate of exponential clustering (Fig. 5) is qualitatively similar to but still slower to the theoretical prediction for the purely divergent case EXP3 (Klyatskin, 2015; Klyatskin & Koshel, 2017; Koshel et al., 2019). Despite the general tendency towards the exponential clustering, the clustering process is significantly affected by the specifics of the

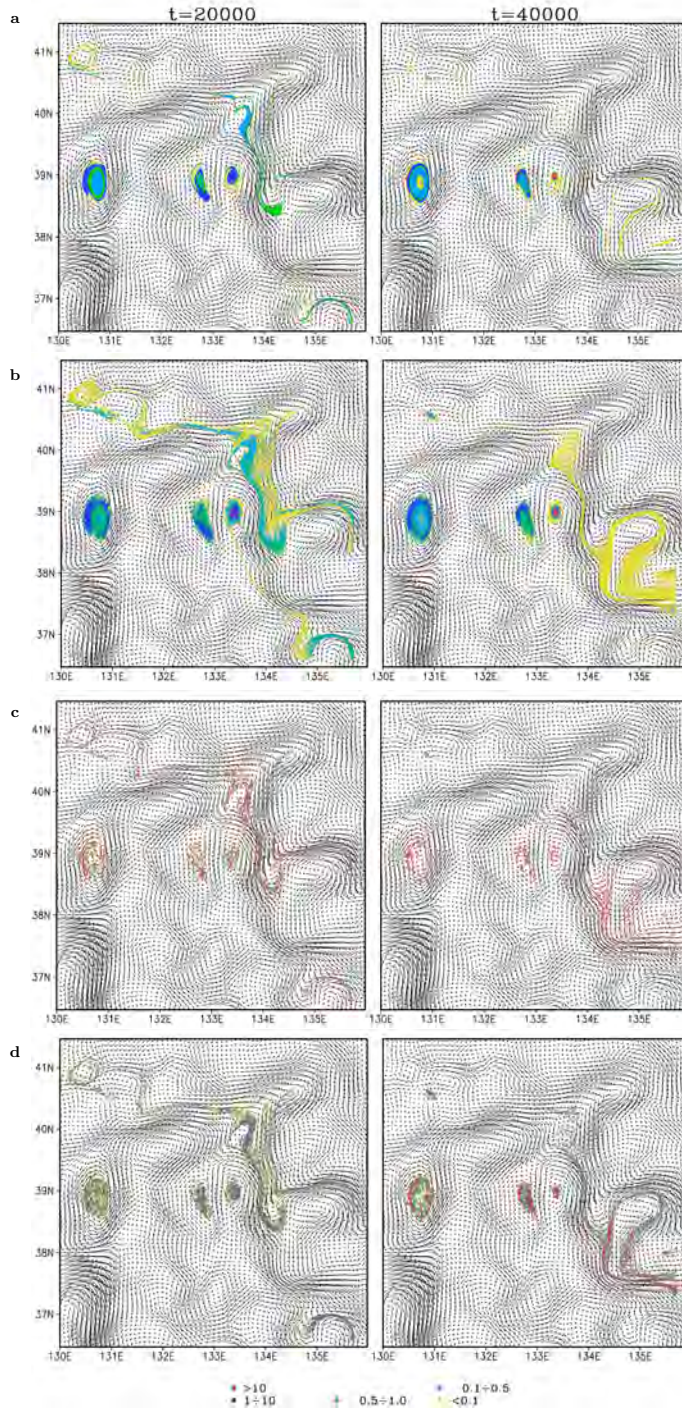


Figure 3: Tracer densities corresponding to (a) EXP1 – regular velocity component, no random velocity, (b) EXP2 – regular plus purely rotational random velocity component, (c) EXP3 – regular plus purely divergent random velocity component, and (d) EXP4 – regular plus mixed rotational and divergent random velocity components ($\gamma = 0.5$). Colour-coded is the dimensionless tracer density; red values indicate the exponential clustering. The tracer advection patterns remain similar: the C_1 -tracer remains bounded to the original deployment site; the A_1 -tracer is redistributed within the cyclone-anticyclone pair; the A_2 -tracer is advected southeastward.

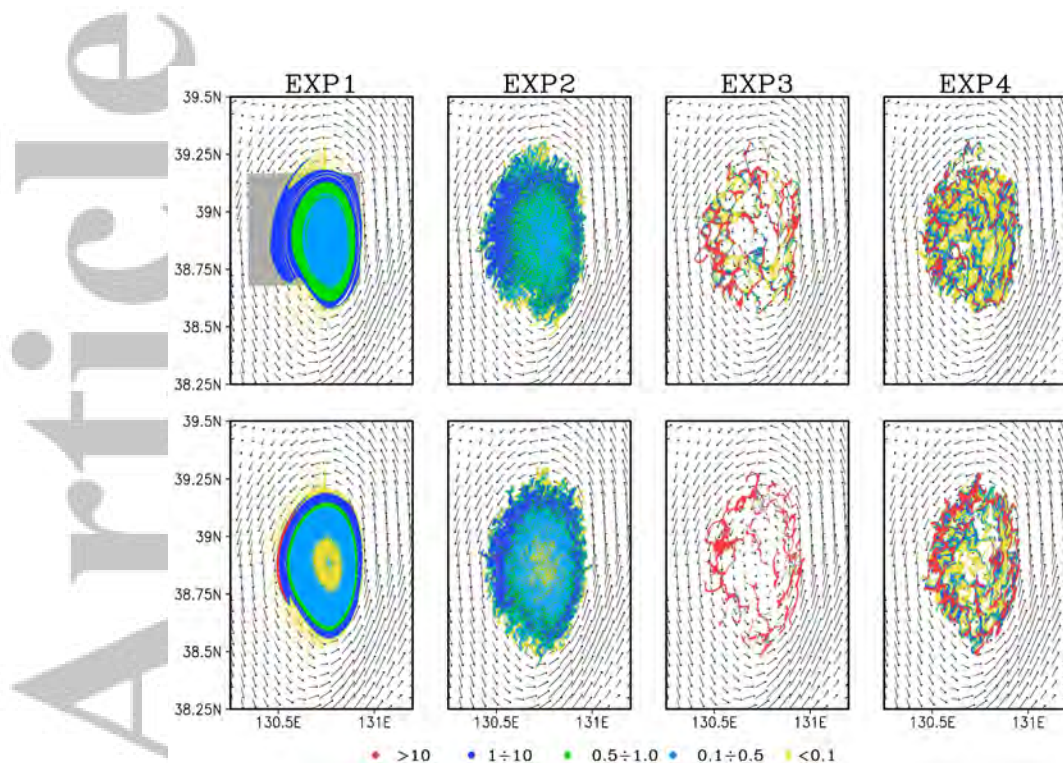


Figure 4: Tracer density for the benchmark experiments. The enlarged region corresponds to C_1 deployment location. Top and bottom rows correspond to consequent dimensionless time instances $t = 20000$ and 40000 , respectively. The rest is as in Fig. 2.

253 regular velocity, as illustrated by different evolution curves for different locations of the
 254 initial tracer deployment (Fig. 5). Formation of clusters can be inhibited by intense shear
 255 in jet-like flows, as can be seen in Fig. 5 for the A_2 case.

256 Changing the random velocity field parameters σ_U and l is similar to changing the
 257 diffusivity. The clustering proxy curves calculated for different sets of the parameters (pur-
 258 ple curve ($\sigma_U = 0.2, l = 0.04$), thin black curve ($\sigma_U = 0.1, l = 0.16$) and other combi-
 259 nations in fig. 5) produce similar shapes of the curves. If D_p is decreased, the cluster-
 260 ing rate slows down for the larger values of the clustering mass (Jacobs et al., 2016); if
 261 D_p is increased, the rate of clustering in the large-time limit decreases; overall, the ef-
 262 fective diffusivity cannot stop or initiate clustering, and only modifies it.

263 4 Conclusions

264 This study was motivated by the well-established phenomenon of clustering, that
 265 is, the development of spatially localised aggregations, here, of floating tracers (e.g., ma-
 266 rine plastic or other pollution, marine biomass) on the ocean surface. The underlying
 267 theory for this phenomenon remains largely undeveloped, except for simple kinematic,
 268 random velocity flows, which are our starting point. The work contributes to a better
 269 understanding of the effects characteristic of the floating tracer as compared to the pas-
 270 sive one. The other novelty is in considering clustering in the velocity field containing
 271 both random and regular (i.e., dynamically constrained) components. The latter com-
 272 ponent comes from a dynamical, realistic, general circulation model of the Japan/East
 273 Sea's region, and it features mesoscale vortices; the former one aims at representing sub-
 274 mesoscale motions unresolved by the dynamical model and simulated by a random kine-
 275 matic model.

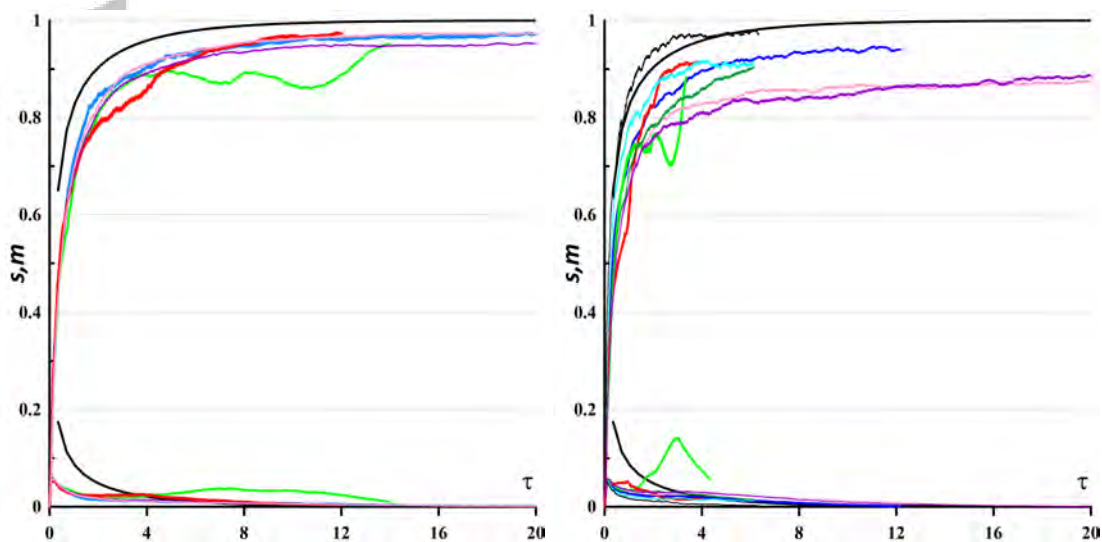


Figure 5: Time series of clustering mass (top curves) and clustering area (bottom curves) for EXP3 (left panel) and EXP4 (right panel) for the tracer deployment locations: C_1 - blue lines, A_1 - red lines, and A_2 - green lines ($\sigma_U = 0.1, l = 0.08$). The black curves show theoretical estimates (11) for the purely divergent case (EXP3). Additional curves correspond to different sets of the parameters (σ_U, l) through (11), and the tracer deployment location C_1 : purple - $D_p = 16D_0$ ($\sigma_U = 0.2, l = 0.04$); thin black - $D_p = \frac{1}{4}D_0$ ($\sigma_U = 0.1, l = 0.16$); light blue - $D_p = D_0$ ($\sigma_U = 0.2, l = 0.16$); pink - $D_p = 4D_0$ ($\sigma_U = 0.1, l = 0.04$); dark green - $D_p = D_0$ ($\sigma_U = 0.05, l = 0.04$). For most of the cases, the exponential nature of clustering is clearly evident.

276 Four experiments with gradually increased influence of the divergent component
 277 of the flow were devised; 3 regions of interest were selected, as represented by typical foot-
 278 prints of the mesoscale eddies: an isolated cyclonic eddy; two anticyclonic eddies; a pair
 279 of cyclonic-anticyclonic eddies. A compelling feature of the presented clustering behaviour
 280 is the widespread distribution of intermittent patterns of floating-tracer clusters within
 281 regions of intense shears, such as vortices and jets. This suggests that real mesoscale ed-
 282 dies in the ocean should also contain similar patterns; although, the relevant observa-
 283 tions are either scarce or with inadequate spatial resolution (see Fig. 1 in (Huntley et
 284 al., 2015) and Fig. 2 in (Lim et al., 2012), which feature intermittent cluster patterns
 285 similar to our model solutions).

286 Upon comparison with the comprehensive study (Jacobs et al., 2016), we agree with
 287 their scenario that the short-time clustering is associated with the submesoscale diver-
 288 gence but argue that the long-term clustering is also due to the submesoscale divergence,
 289 while the mesoscales do not directly induce clustering but rather advect already formed
 290 clusters into larger aggregations. This is asserted using the statistical topography tech-
 291 niques showing that the rate of clustering does not change in time and is largely inde-
 292 pendent of the spatial inhomogeneities, such as given by mesoscale eddies.

293 A serious challenge for further comparison between the model solution and obser-
 294 vations is disentangling of specific contributions of the rotational and divergent veloc-
 295 ity components that are shown to be essential for the rate and intensity of the cluster-
 296 ing process.

297 Acknowledgments

298 This study was partially supported by the POI FEB RAS Program “Mathematical sim-
 299 ulation and analysis of dynamical processes in the ocean” (AAAA–A117030110034–
 300 7) and by the Russian Foundation for Basic Research projects 19 – 55 – 10001, 20 –
 301 05–00083. EAR and PB were supported by the NERC grant *NE/R011567/1* and by
 302 the Royal Society Exchange Grant *IEC/R2/181033*. The contribution of KVK in ob-
 303 taining the analytical estimates was supported by the Russian Scientific Foundation project
 304 19–17–00006. PB also gratefully acknowledges support from the NERC grant *NE/T002220/1*
 305 and the Leverhulme grant *RPG–2019–024*, as well as the hospitality of the Shirshov
 306 Institute of Oceanology. The numerical simulation outputs were obtained using the Shared
 307 Resource Center “Far Eastern Computing Resource” IACP FEB RAS ([https://www.cc](https://www.cc.dvo.ru)
 308 [.dvo.ru](https://www.researchgate.net/publication/336133063_dataset_for_Geophysical_Research_Letters)). Data are available [https://www.researchgate.net/publication/336133063](https://www.researchgate.net/publication/336133063_dataset_for_Geophysical_Research_Letters)
 309 [_dataset_for_Geophysical_Research_Letters](https://www.researchgate.net/publication/336133063_dataset_for_Geophysical_Research_Letters).

310 References

- 311 Barbosa Aguiar, A. C., Peliz, A., & Carton, X. (2013). A census of meddies in a
 312 long-term high-resolution simulation. *Prog. Oceanogr.*, *116*, 80–94. doi: 10
 313 .1016/j.pocean.2013.06.016
- 314 Berta, M., Griffa, A., Özgökmen, T. M., & Poje, A. C. (2016). Submesoscale evolu-
 315 tion of surface drifter triads in the gulf of mexico. *Geophys. Res. Lett.*, *43*(22),
 316 11,751–11,759. doi: 10.1002/2016GL070357
- 317 Berti, S., Santos, F. A. D., Lacorata, G., & Vulpiani, A. (2011). Lagrangian drifter
 318 dispersion in the southwestern atlantic ocean. *J. Phys. Oceanogr.*, *41*(9), 1659–
 319 1672. doi: 10.1175/2011JPO4541.1
- 320 Cedarholm, E. R., Rypina, I. I., Macdonald, A. M., & Yoshida, S. (2019). Investi-
 321 gating subsurface pathways of fukushima cesium in the northwest pacific. *Geo-*
 322 *phys. Res. Lett.*, *46*(12), 6821–6829. doi: 10.1029/2019GL082500
- 323 Chelton, D. B., Schlax, M. G., & Samelson, R. M. (2011). Global observations of
 324 nonlinear mesoscale eddies. *Prog. Oceanogr.*, *91*(2), 167–216.
- 325 Chelton, D. B., Schlax, M. G., Samelson, R. M., & de Szoeke, R. A. (2007). Global

- 326 observations of large oceanic eddies. *Geophys. Res. Lett.*, *34*, L15606.
- 327 Cozar, A., Echevarria, F., Gonzalez-Gordillo, J. I., Irigoien, X., Ubeda, B.,
328 Hernandez-Leon, S., ... Duarte, C. M. (2014). Plastic debris in the open
329 ocean. *Proceedings of the National Academy of Sciences*, *111*, 10239-10244.
330 doi: 10.1073/pnas.1314705111
- 331 Dauhajre, D. P., McWilliams, J. C., & Renault, L. (2019). Nearshore lagrangian
332 connectivity: Submesoscale influence and resolution sensitivity. *J. Geophys.*
333 *Res.: Oceans*, *124*(7), 5180–5204. doi: 10.1029/2019JC014943
- 334 Diansky, N. A., Stepanov, D. V., Gusev, A. V., & Novotryasov, V. V. (2016). Role
335 of wind and thermal forcing in the formation of the water circulation variabil-
336 ity in the Japan/East Sea Central Basin in 1958–2006. *Izvestiya, Atmospheric*
337 *and Oceanic Physics*, *52*, 207–216. doi: 10.1134/S0001433816010023
- 338 Haza, A. C., Özgökmen, T. M., & Hogan, P. (2016). Impact of submesoscales on
339 surface material distribution in a gulf of mexico mesoscale eddy. *Ocean Mod-*
340 *elling*, *107*, 28 - 47. doi: <https://doi.org/10.1016/j.ocemod.2016.10.002>
- 341 Huntley, H. S., Lipphardt Jr., B. L., Jacobs, G., & Kirwan Jr., A. D. (2015). Clus-
342 ters, deformation, and dilation: Diagnostics for material accumulation regions.
343 *J. Geophys. Res.: Oceans*, *120*(10), 6622-6636. doi: 10.1002/2015JC011036
- 344 Isichenko, M. B. (1992). Percolation, statistical topography, and transport in ran-
345 dom media. *Rev. Mod. Phys.*, *64*, 961–1043. doi: 10.1103/RevModPhys.64
346 .961
- 347 Jacobs, G. A., Huntley, H. S., Kirwan Jr., A. D., Lipphardt Jr., B. L., Campbell,
348 T., Smith, T., ... Bartels, B. (2016). Ocean processes underlying surface
349 clustering. *Journal of Geophysical Research: Oceans*, *121*(1), 180-197. doi:
350 10.1002/2015JC011140
- 351 Kloeden, P., & Platen, E. (1992). *Numerical solution of stochastic differential equa-*
352 *tions*. Springer, Berlin.
- 353 Klyatskin, V. I. (1994). Statistical description of the diffusion of a passive tracer in a
354 random velocity field. *Physics-Uspelki*, *37*, 501–513.
- 355 Klyatskin, V. I. (2015). *Stochastic equations: Theory and applications in acous-*
356 *tics, hydrodynamics, magnetohydrodynamics, and radiophysics* (Vols. 1,2).
357 Springer.
- 358 Klyatskin, V. I., & Koshel, K. (2017). Impact of diffusion on surface clustering
359 in random hydrodynamic flows. *Phys. Rev. E*, *95*, 013109. doi: 10.1103/
360 PhysRevE.95.013109
- 361 Klyatskin, V. I., & Koshel, K. V. (2000). The simplest example of the development
362 of a cluster-structured passive tracer field in random flows. *Physics-Uspelki*,
363 *170*, 771–778.
- 364 Koshel, K. V., & Alexandrova, O. V. (1999). Some results of a numerical mod-
365 eling of the diffusion of passive tracers in a random field of velocities. *Izv. At-*
366 *mos. Ocean. Phys.*, *35*, 578–588.
- 367 Koshel, K. V., Ryzhov, E. A., & Zhmur, V. V. (2013). Diffusion-affected passive
368 scalar transport in an ellipsoidal vortex in a shear flow. *Nonlin. Processes Geo-*
369 *phys.*, *20*, 437–444. doi: 10.5194/npg-20-437-2013
- 370 Koshel, K. V., Stepanov, D. V., Ryzhov, E. A., Berloff, P., & Klyatskin, V. I.
371 (2019). Clustering of floating tracers in weakly divergent velocity fields. *Physi-*
372 *cal Review E*, *100*. doi: 10.1103/PhysRevE.100.063108
- 373 Law, K. L., Moret-Ferguson, S., Maximenko, N. A., Proskurowski, G., Pea-
374 cock, E. E., Hafner, J., & Reddy, C. M. (2010). Plastic accumulation
375 in the north atlantic subtropical gyre. *Science*, *329*, 1185-1188. doi:
376 10.1126/science.1192321
- 377 Lim, J.-H., Son, S., Park, J.-W., Kwak, J. H., Kang, C.-K., Son, Y. B., ... Lee,
378 S. H. (2012). Enhanced biological activity by an anticyclonic warm eddy
379 during early spring in the east sea (japan sea) detected by the geosta-
380 tionary ocean color satellite. *Ocean Science Journal*, *47*, 377-385. doi:

- 381 10.1007/s12601-012-0035-1
- 382 Martínez, E., Maamaatuaiahutapu, K., & Taillandier, V. (2009). Floating marine
383 debris surface drift: Convergence and accumulation toward the south pacific
384 subtropical gyre. *Marine Pollution Bulletin*, *58*, 1347–1355.
- 385 Martínez-Moreno, J., Hogg, A. M., Kiss, A. E., Constantinou, N. C., & Morrison,
386 A. K. (2019). Kinetic energy of eddy-like features from sea surface altime-
387 try. *Journal of Advances in Modeling Earth Systems*, *11*(10), 3090–3105. doi:
388 10.1029/2019MS001769
- 389 Maximenko, N., Hafner, J., & Niiler, P. (2012). Pathways of marine debris derived
390 from trajectories of lagrangian drifters. *Marine Pollution Bulletin*, *65*(1-3),
391 51–62. doi: 10.1016/j.marpolbul.2011.04.016
- 392 McComb, W. D. (1990). *The physics of fluid turbulence* (Vol. 25). Oxford: Claren-
393 don Press.
- 394 McWilliams, J. C. (2008). The nature and consequences of oceanic eddies. In *Ocean*
395 *modeling in an eddying regime* (p. 5-15). American Geophysical Union (AGU).
396 doi: 10.1029/177GM03
- 397 McWilliams, J. C. (2016). Submesoscale currents in the ocean. *Proc. R. Soc. A*,
398 *472*, 20160117. doi: 10.1098/rspa.2016.0117
- 399 Ohlmann, J. C., Romero, L., Palls-Sanz, E., & Perez-Brunius, P. (2019). Anisotropy
400 in coastal ocean relative dispersion observations. *Geophys. Res. Lett.*, *46*(2),
401 879–888. doi: 10.1029/2018GL081186
- 402 Okubo, A. (1980). *Diffusion and ecological problems: Mathematical models* (Vol. 10).
403 Berlin: Springer-Verlag.
- 404 Olascoaga, M. J., Beron-Vera, F. J., Haller, G., Trinanés, J., Iskandarani, M.,
405 Coelho, E. F., ... Valle-Levinson, A. (2013). Drifter motion in the Gulf of
406 Mexico constrained by altimetric Lagrangian coherent structures. *Geophys.*
407 *Res. Lett.*, *40*, 6171–6175. doi: 10.1002/2013GL058624
- 408 Prants, S. V., Budyansky, M. V., & Uleysky, M. Y. (2018). How eddies gain, retain,
409 and release water: A case study of a hokkaido anticyclone. *J. Geophys. Res.:
410 Oceans*, *123*(3), 2081–2096.
- 411 Samelson, R. M. (2013). Lagrangian motion, coherent structures, and lines of persis-
412 tent material strain. *Annu. Rev. Mar. Sci.*, *5*, 137–163. doi: 10.1146/annurev-
413 -marine-120710-100819
- 414 Schroeder, K., Chiggiato, J., Haza, A. C., Griffa, A., Özgökmen, T. M., Zanasca,
415 P., ... Trees, C. (2012). Targeted lagrangian sampling of submesoscale
416 dispersion at a coastal frontal zone. *Geophys. Res. Lett.*, *39*(11). doi:
417 10.1029/2012GL051879
- 418 Stepanov, D. V., Diansky, N. A., & Fomin, V. V. (2018). Eddy energy sources and
419 mesoscale eddies in the Sea of Okhotsk. *Ocean Dynamics*, *68*, 825–845. doi:
420 10.1007/s10236-018-1167-3
- 421 Stepanov, D. V., Diansky, N. A., & Novotryasov, V. V. (2014). Numerical simu-
422 lation of water circulation in the central part of the Sea of Japan and study
423 of its long-term variability in 1958–2006. *Izvestiya, Atmospheric and Oceanic
424 Physics*, *50*, 73–84. doi: 10.1134/S0001433813050149
- 425 Väli, G., Zhurbas, V. M., Laanemets, J., & Lips, U. (2018). Clustering of floating
426 particles due to submesoscale dynamics: a simulation study for the gulf of fin-
427 land, baltic sea. *Fundamentalnaya i Prikladnaya Gidrofizika*, *11*(2), 21–35. doi:
428 10.7868/S2073667318020028
- 429 Wang, Y., Olascoaga, M. J., & Beron-Vera, F. J. (2015). Coherent water transport
430 across the south atlantic. *Geophys. Res. Lett.*, *42*(10), 4072–4079. doi: 10.1002/
431 2015GL064089
- 432 Zhong, Y., & Bracco, A. (2013). Submesoscale impacts on horizontal and vertical
433 transport in the gulf of mexico. *J. Geophys. Res.: Oceans*, *118*(10), 5651–5668.
434 doi: 10.1002/jgrc.20402

fig1.

Accepted Article

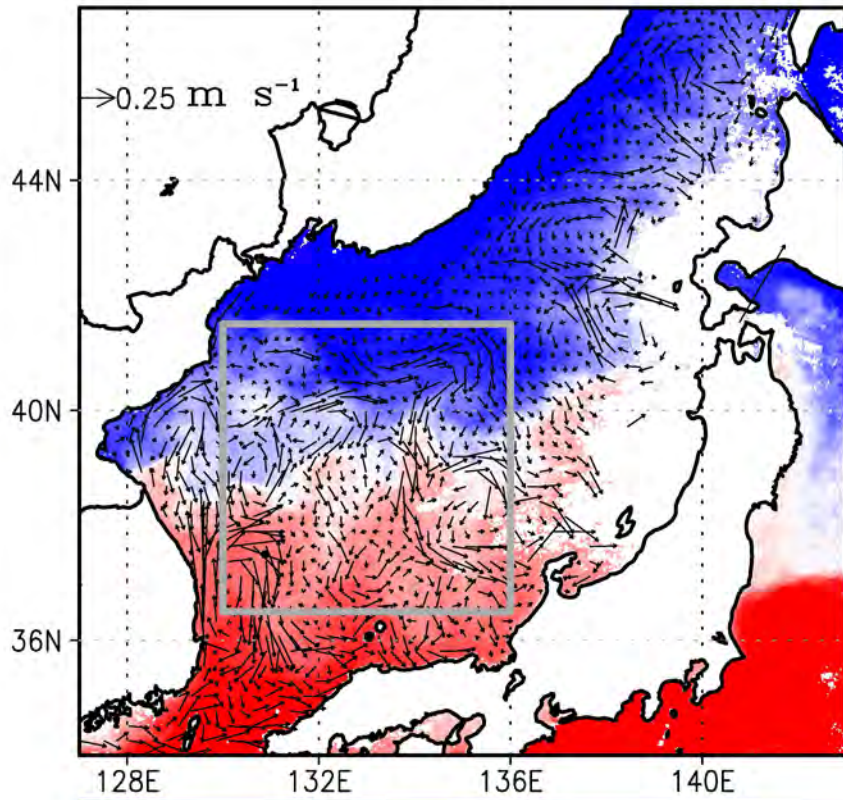
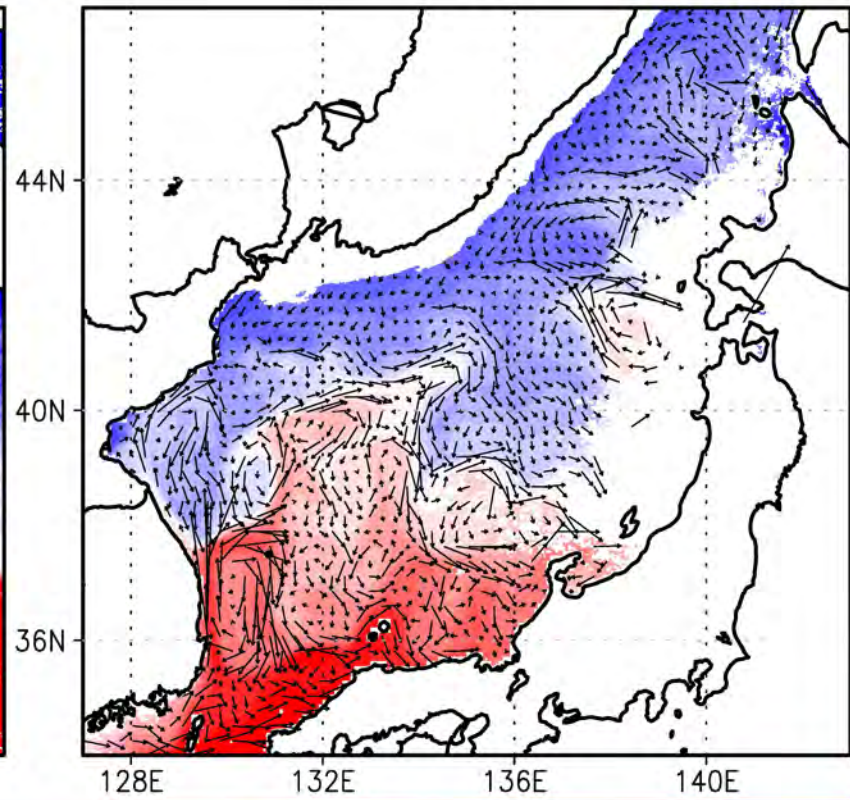
a**b**

fig2.

Accepted Article

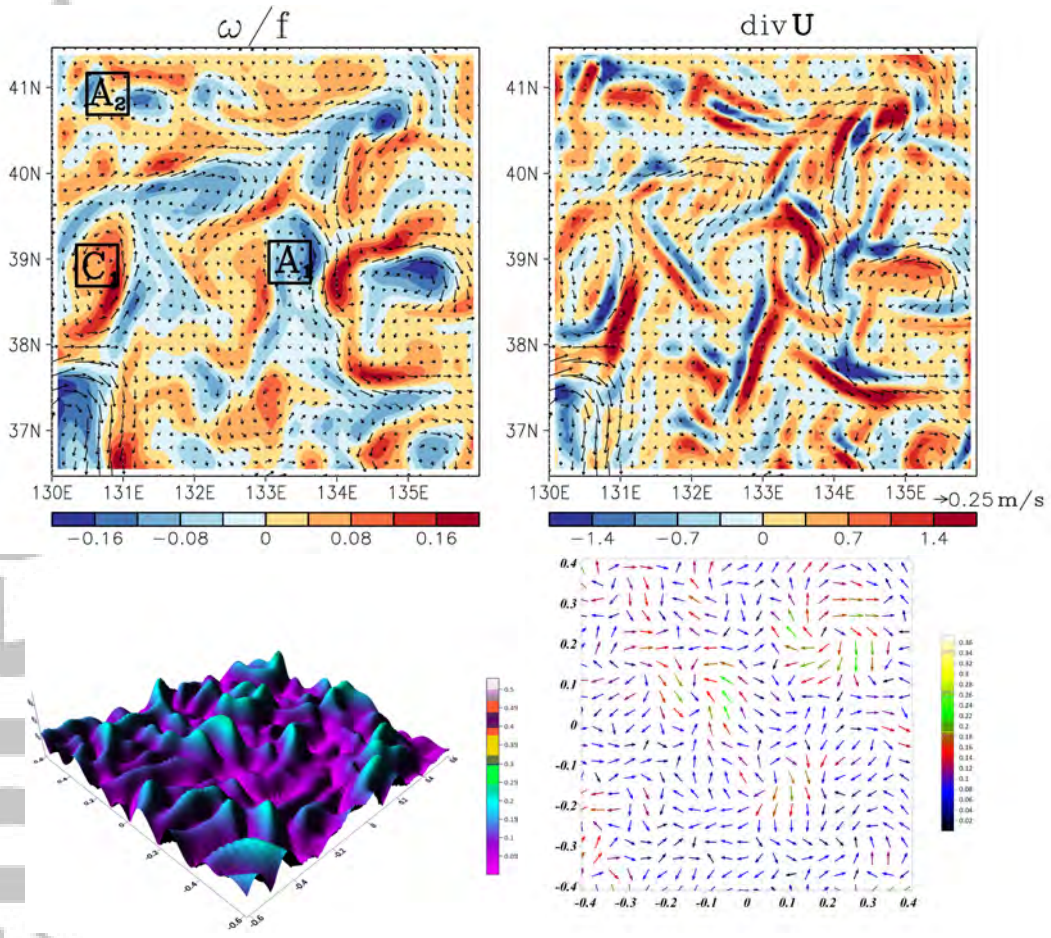


fig3.

Accepted Article

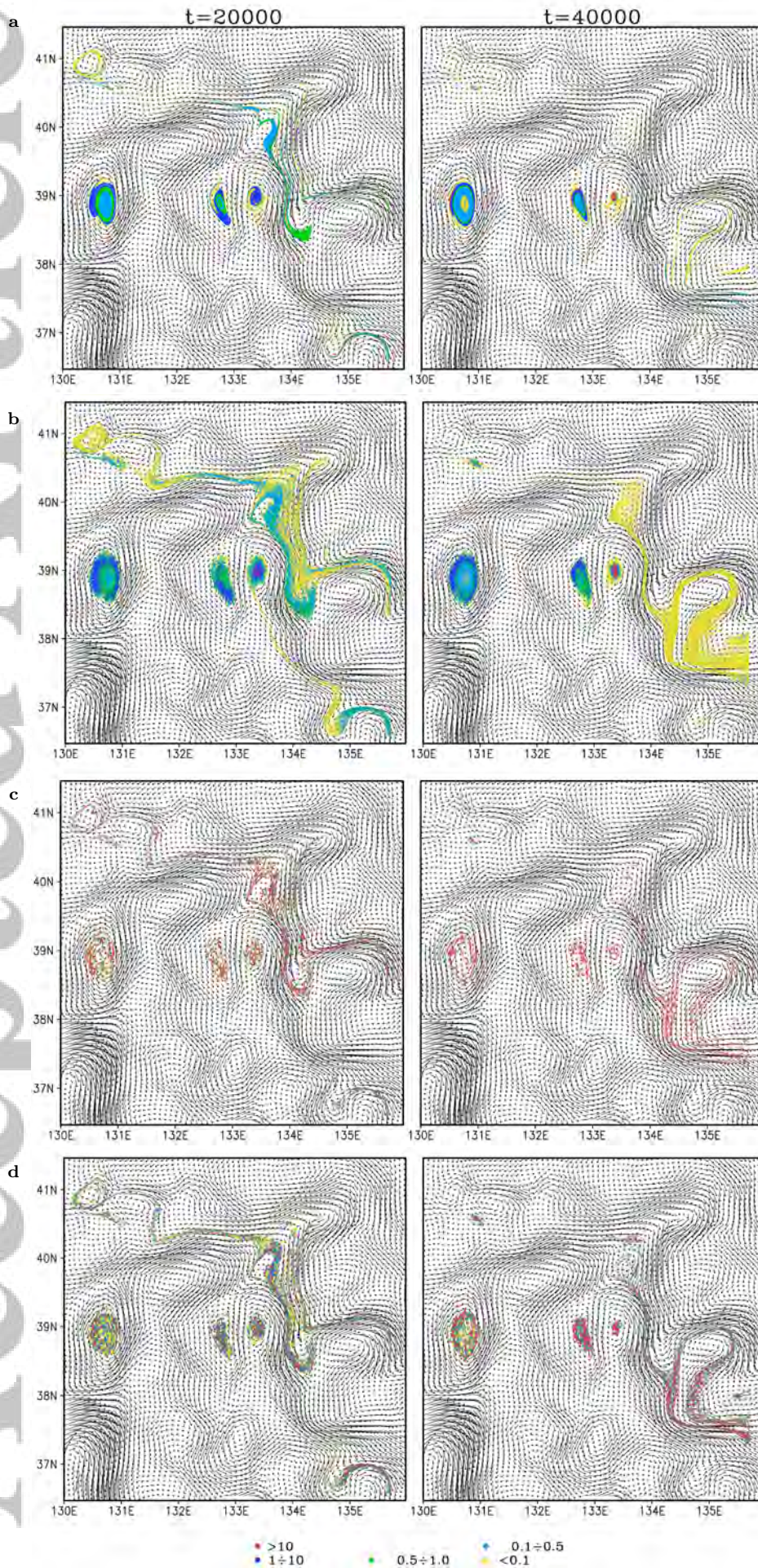


fig4.

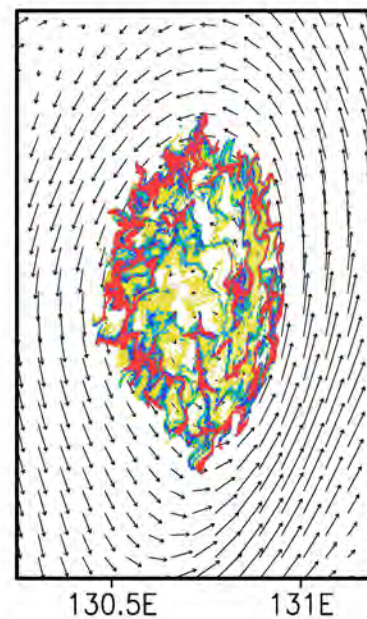
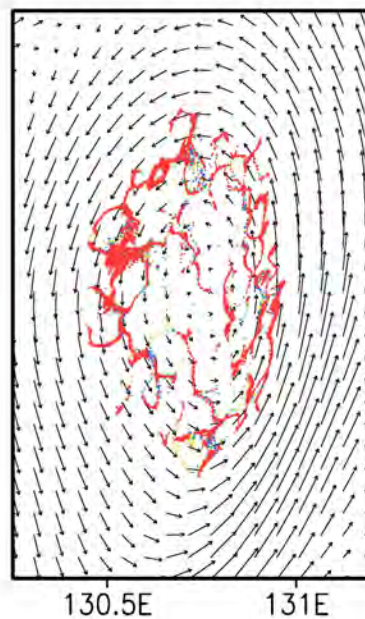
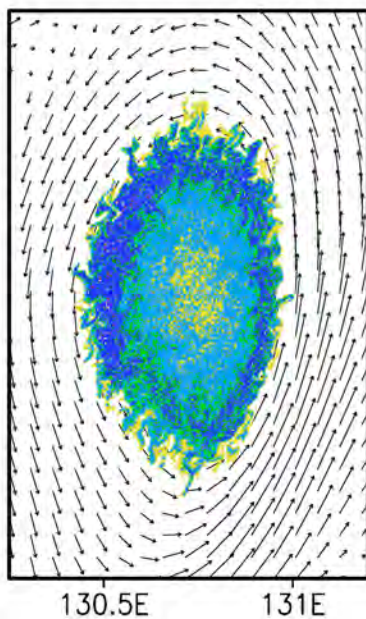
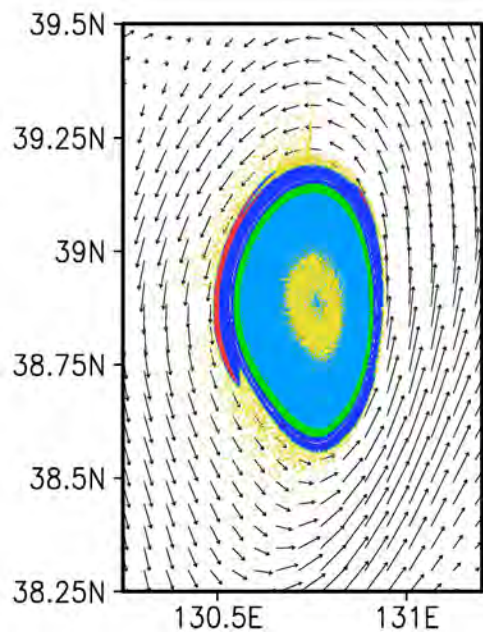
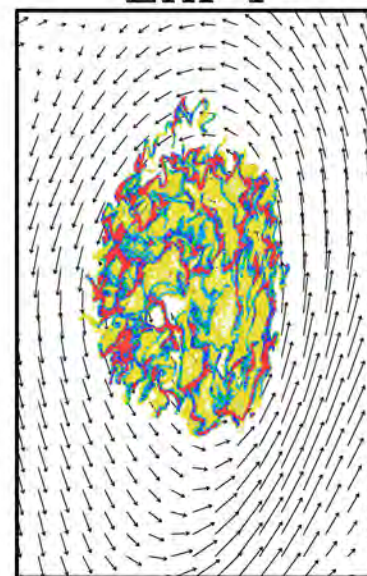
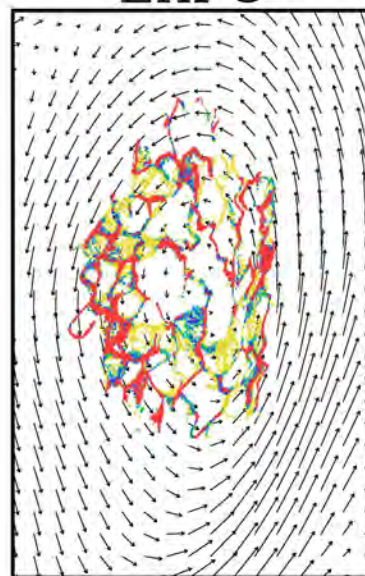
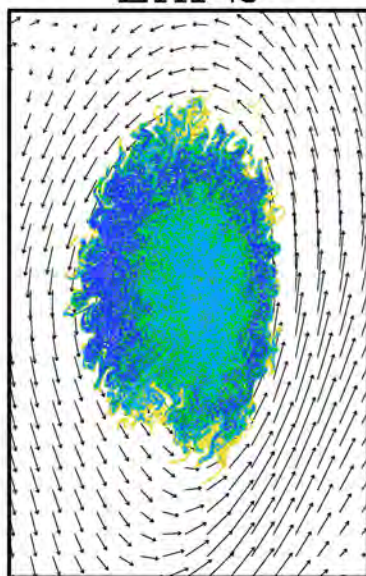
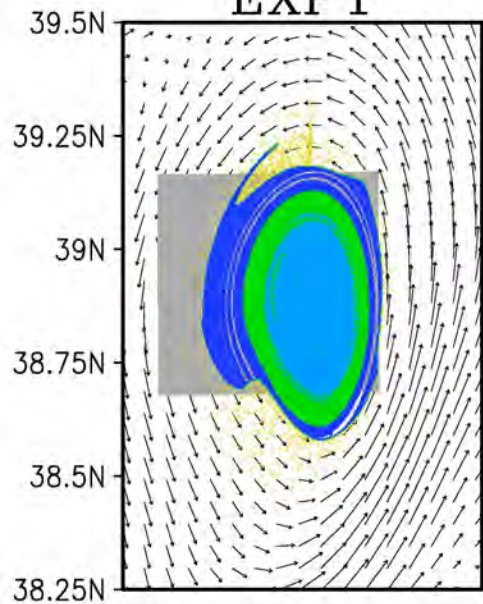
Accepted Article

EXP 1

EXP 2

EXP 3

EXP 4



• > 10

• 1 ÷ 10

• 0.5 ÷ 1.0

• 0.1 ÷ 0.5

• < 0.1

fig5.

Accepted Article

